optica

Self-starting bi-chromatic $LiNbO_3$ soliton microcomb: supplementary material

YANG HE[1,†], QI-FAN YANG[2,†], JINGWEI LING[3], RUI LUO[3], HANXIAO LIANG[1], MINGXIAO LI[1], BOQIANG SHEN[2], HEMING WANG[2], KERRY VAHALA[2,4], AND QIANG LIN[1,3,5]

[1] Department of Electrical and Computer Engineering, University of Rochester, Rochester, NY 14627
[2] T.J. Watson Laboratory of Applied Physics, California Institute of Technology, Pasadena, California 91125
[3] Institute of Optics, University of Rochester, Rochester, NY 14627
[†] These authors contribute equally to this work.
[4] e-mail: vahala@caltech.edu
[5] e-mail: qiang.lin@rochester.edu

Published 30 August 2019

This document provides supplementary information to the article "Self-starting bi-chromatic $LiNbO_3$ soliton microcomb," https://doi.org/10.1364/OPTICA.6.001138. In this supplement, detailed information is provided on the following: the device design, the experimental setup, device fabrication and characterization, the numeric modeling of soliton comb generation with analysis of self-starting mode locking, and the characterization of key device parameters.

DEVICE DESIGN AND PROPERTIES

Control of group-velocity dispersion (GVD) in the anomalous dispersion regime is crucial for generating soliton Kerr frequency combs. Waveguide design is possible by numerical modeling of waveguide cross sections using a finite element method solver (COMSOL) . Figure S1(a) shows the simulated GVD curve for different waveguide widths where a diagram of the waveguide cross section is provided in Fig. S1(b). Other waveguide dimensions are provided in the figure caption. A waveguide width of 2.0 μm was chosen because it provides anomalous GVD with a reasonably small magnitude over a broad spectral band, but not so small as to be sensitive to fabrication error. As shown in Fig. 1(d) of the main text, the GVD of the fabricated device is close to prediction from modeling. Based on the simulation, the effective refractive index n_0 of the device is determined to be around 2.0 at 1555 nm. The microring is side coupled to a pulley waveguide with a width of 1.4 μm and with a gap of 0.7 μm as shown in Fig. 1(b) of the main text.

Figure S1(c) shows the transmission spectrum of the device for coupling to the quasi-TE polarization (where the electric field of optical modes predominantly lies in the device plane.). Fig. S1(d) is a higher resolution scan of a cavity mode (indicated by the red arrow in Fig. S1(c)) and shows that the device exhibits a high optical Q of 2.2×10^6 for the loaded cavity. As shown in Fig. S1(c), the device exhibits good external coupling over a broad spectrum in the telecom band. However, it has very low external coupling efficiency for the second harmonic signal as evident in the images of Fig. 2 of the main text, since it was designed for operation in the telecom band. The coupling efficiency at the second harmonic band can be significantly improved with future optimization of the coupling-waveguide design.

DEVICE FABRICATION

The device was fabricated on a 600-nm-thick congruent LN thin film sitting on a 3 μm-thick buried silicon oxide layer. The ZEP-520A resist was used as a mask to define the device structure, which was patterned by electron-beam lithography. After the device pattern was defined, the LN layer was etched down by about 410 nm, via an Ar-ion milling process, forming a waveguide cross section as schematically shown in Fig. S1(b) (as well as in Fig. 1(c) of the main text). Finally, the facet of the chip was polished to obtain good fiber-to-chip light coupling.

EXPERIMENT SETUP AND DEVICE CHARACTERIZATION

Figure S2(a) shows the schematic of the experimental testing setup. A continuous-wave (CW) telecom-band tunable laser was used as the pump laser. The laser power was boosted

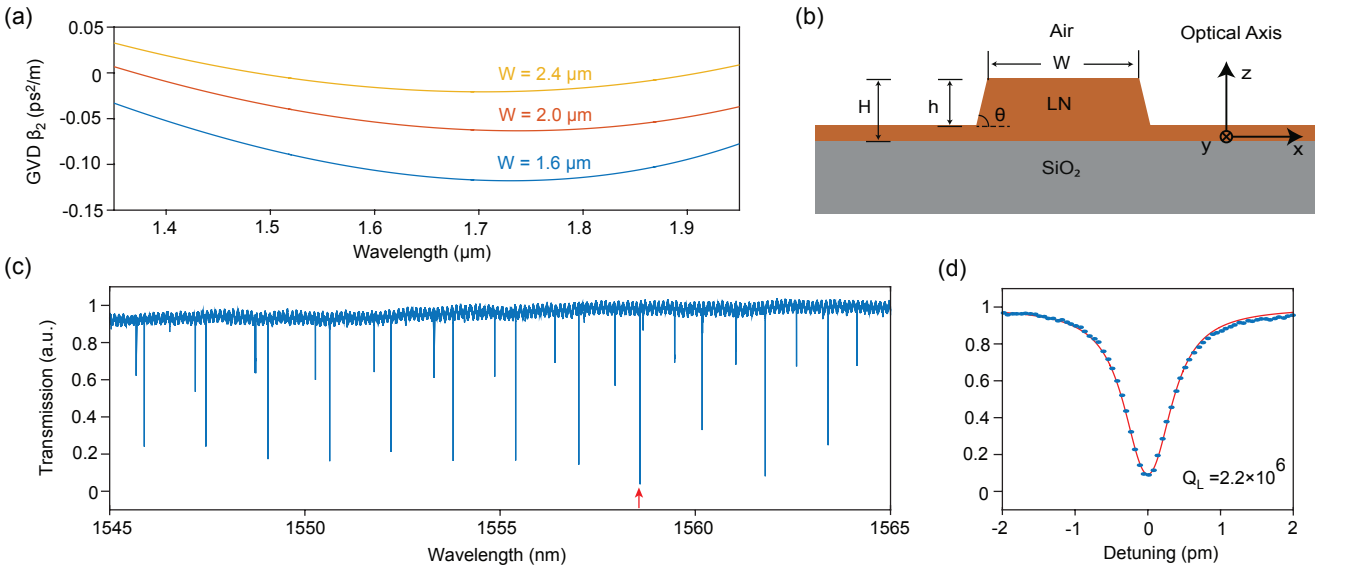

Fig. S1. Dispersion engineering and device characterization. (a) Simulated GVD curves for the fundamental quasi-TE mode of a straight waveguide with different waveguide widths (W). **(b)** Schematic of the waveguide cross section, with parameters: H = 600 nm, $h = 410$ nm, and $\theta = 75°$. **(c)** Normalized transmission spectrum of the device. **(d)** High resolution transmission spectrum of a fundamental quasi-TE mode, indicated as red arrow in (**c**). The experiment data are shown as blue dots and the fitting curve is shown in red.

by an erbium-doped fiber amplifier (EDFA) whose amplified spontaneous emission (ASE) noise was suppressed by a tunable optical filter. The polarization of the laser was adjusted by a polarization controller (PC) to match the quasi-TE polarization of the cavity mode. The pump light was coupled to the device chip through a lensed fiber. The comb light output from the device chip was collected by another lensed fiber. A fiber Bragg grating (FBG) was used to separate the pump light from the frequency comb, and the pump light (directed to the drop port in the schematic) was photodetected (PD) to monitor the cavity transmission (Fig. S2(b),(c)). The comb light transmitted to the through port was measured using a photodetector (Fig. S2(d),(e)), an optical spectrum analyzer (OSA), and a frequency-resolved optical gating (FROG) for soliton temporal waveform characterization. In order to reach the minimum working power of FROG, an EDFA boosted the comb power and a dispersion compensation unit (DCU) was used to compensate the dispersion introduced by the EDFA. As the repetition rate of the device is too large to be measured by an electrical spectrum analyzer (ESA), the coherence of individual comb lines was studied by heterodyning with a reference CW laser and measuring the electrical spectrum with an ESA. The generated second harmonic of the Kerr soliton was characterized from the light scattered from the device into free space. The scattered light was collected by an imaging microscope whose output was either recorded by a CMOS camera (spectral response: 400-1000 nm) or was delivered, via a multimode fiber (MMF), to a spectrometer that covers the near infrared spectral band around 700-900 nm.

The pump transmission (Fig. S2(b),(c)) and comb power (Fig. S2(d),(e)) are monitored for pump frequency scanning in both tuning directions. When the pump frequency is scanned from red-detuned frequencies towards the resonance, the comb power versus tuning shows discrete steps (Fig. S2(d)), a signature of soliton mode locking. The single-soliton and two-soliton states shown in Fig. 1(g) and (h) of the main text are recorded from the first and second comb-power steps, respectively. On the other hand, when the pump frequency is scanned from blue-detuned frequencies across the resonance, the step formation is not observed until the pump frequency enters into the red-detuned regime (Fig. S2(e)), at which point the power steps correspond to the first few steps in Fig. S2(d).

DISPERSION CHARACTERIZATION

To characterize the GVD of the device, we measured the resonance frequency ω_μ of the soliton forming mode family as a function of relative mode number μ, referred to a reference resonance at ω_0 ($\mu = 0$ corresponds to a cavity mode at a wavelength around 1558.7 nm). The cavity resonance frequency ω_μ is described by a Taylor series around a reference resonance ω_0 [1], $\omega_\mu = \omega_0 + \mu D_1 + \frac{1}{2}\mu^2 D_2 + \frac{1}{6}\mu^3 D_3 + \cdots$, where $D_1/(2\pi)$ is the FSR around ω_0 and D_2 is related to the GVD β_2 as $D_2 = -\frac{c}{n}D_1^2\beta_2$. Figure 1(d) of the main text shows $D_{\text{int}} \equiv \omega_\mu - \omega_0 - \mu D_1$. Fitting the experimental data, we obtained $D_1/(2\pi) = 199.7$ GHz and $D_2/(2\pi) = 1.76$ MHz, corresponding to $\beta_2 = -0.047$ ps^2/m.

ON THE THEORETICAL MODELING OF SELF-STARTING SOLITON MODE LOCKING

A. The Lugiator-Lefever equation

The generation of a Kerr frequency comb inside a microresonator is well described by the Lugiato-Lefever equation (LLE) [2, 3]

$$t_R \frac{\partial A(t,\tau)}{\partial t} = \Big[-\alpha - i\delta_0 + iL\sum_{k\geq 2}\frac{\beta_k}{k!}(i\frac{\partial}{\partial\tau})^k + i\gamma L|A|^2\Big]A + \sqrt{\theta}A_{in}. \tag{S1}$$

where A is the optical field such that $|A|^2$ is normalized to optical power. Also, t_R is the roundtrip time, L is the cavity length, $\alpha = (\alpha_0 + \theta)/2$ is the total loss (where α_0 is the intrinsic absorption coefficient and θ is the transmission coefficient determined

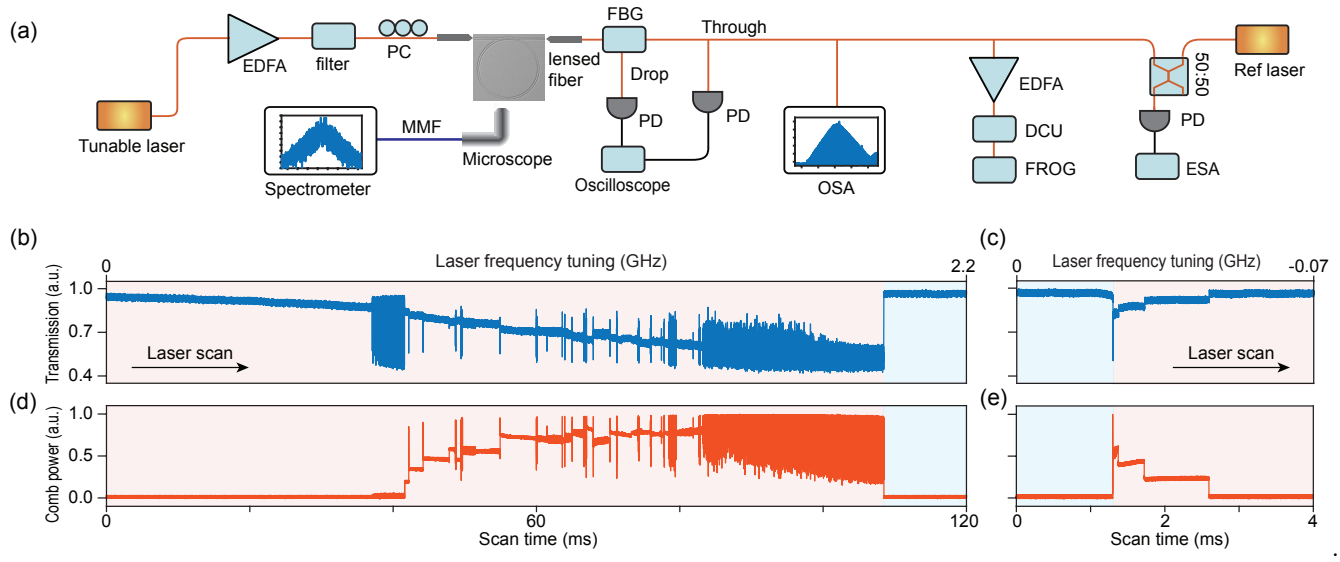

Fig. S2. Testing setup and comb characterization. (a) Schematic of the experimental testing setup. **(b) and (c)** Resonator transmission when the pump laser frequency is scanned from red to blue (**b**) and blue to red (**c**) across the pump resonance. The laser power is 33 mW on chip. **(d) and (e)** Comb power versus frequency tuning corresponding to (**b**) and (**c**), respectively. The shaded red and blue regions indicate the approximate red-detuned and blue-detuned frequency regimes, respectively. (**d**) and (**e**) are the same as Fig. 1(e) and (f) in the main text. They are re-plotted here to have a direction comparison with the resonance transmission spectrum in (**b**) and (**c**).

by the coupling between the resonator and the coupling waveguide), β_k is the k^{th}-order dispersion coefficient, $\gamma = \frac{n_2\omega_0}{cA_{\text{eff}}}$ is the nonlinear parameter (where n_2 is Kerr nonlinear coefficient and A_{eff} is the effective mode area), and $\delta_0 = 2\pi l - \phi_0$ is the phase detuning between the l^{th}-order reference resonance mode and the driving field. In Eq. (S1), τ is the *fast* time variable used to describe the detailed dynamics of comb within a round-trip time, and t is the *slow* time variable used to describe the comb evolution over a time scale longer than the round-trip time [3].

Considering the periodic condition of a ring resonator for the intra-cavity field, the field $A^{(m+1)}(0,\tau)$ at the beginning of the next roundtrip will be the summation of input filed A_{in} and the original filed $A^{(m)}(L,\tau)$ after a roundtrip length L [3]:

$$A^{(m+1)}(0,\tau) = \sqrt{\theta}A_{in} + \sqrt{1-\theta}A^{(m)}(L,\tau)e^{i\phi_0}. \tag{S2}$$

In general, the properties of a microresonator are well described by device parameters such as optical Q, photon decay rate Γ_t (related to optical Q as $\Gamma_t = \frac{\omega_0}{Q}$), and the laser-cavity frequency detuning $\Delta_0 = \omega_p - \omega_0$ (where ω_p is the pump frequency and ω_0 is the frequency of the passive cavity mode being pumped and in the absence of the optical power). Therefore, Equation (S1) can be written in a more intuitive way as

$$\frac{\partial A(t,\tau)}{\partial t} = \Big[-\frac{\Gamma_t}{2} + i\Delta_0 + iv_g\sum_{k\geq 2}\frac{\beta_k}{k!}(i\frac{\partial}{\partial\tau})^k + i\gamma v_g|A|^2\Big]A + \sqrt{\frac{\theta}{t_R^2}}A_{in}, \tag{S3}$$

where $v_g = \frac{L}{t_R}$ is the group velocity, Δ_0 is related to δ_0 as $\Delta_0 = -\frac{\delta_0}{t_R}$, and Γ_t is related to α as $\Gamma_t = 2\alpha v_g$. The final soliton state will be determined by the detuning Δ_0, the dispersion β_k, Kerr nonlinearity n_2, and the optical Q of the loaded cavity ($Q = \frac{\omega_0}{\Gamma_t}$) [4].

B. Description and incorporation of the photorefractive effect

Equation (S3) (or Equation (S1)) includes only the optical Kerr effect and the dispersion effect. It is not adequate to describe our device where other nonlinear effects are expected to play important roles. A dominant one is the photorefractive effect [5], where the refractive index of the device material decreases with increased optical power inside the resonator, leading to a blue shift of the cavity resonance. The photorefractive effect is essentially an electro-optic effect induced by the space charge electric field produced by photo-excitation (to certain defects) [5]. Therefore, the photorefractive-induced resonance tuning can be described as $\delta\omega_0 = g_E E_{sp}$ where g_E represents the electro-optic coupling coefficient and E_{sp} represents the induced space-charge electric field [6].

As shown below, the photorefractive effect responds very slowly to changes in cavity optical power in comparison to both the roundtrip time (~5 ps) and the photon lifetime (~1.8 ns) of the resonator. Therefore, the photorefractive-induced resonance tuning can be described in an adiabatic fashion. As such, the laser-cavity detuning term in Eq. (S3), Δ_0, is replaced by $\Delta = \Delta_0 - \delta\omega_0 = \Delta_0 - g_E E_{sp}$, and Eq. (S3) now becomes

$$\frac{\partial A(t,\tau)}{\partial t} = \Big[-\frac{\Gamma_t}{2} + i\Delta_0 - ig_E E_{sp} + iv_g\sum_{k\geq 2}\frac{\beta_k}{k!}(i\frac{\partial}{\partial\tau})^k + i\gamma v_g|A|^2\Big]A + \sqrt{\frac{\theta}{t_R^2}}A_{in}. \tag{S4}$$

Furthermore, the dynamics of the space-charge electric field can be described by a simple excitation-relaxation process [6].

$$\frac{d(E_{sp})}{dt} = -\Gamma_{sp}E_{sp} + \eta_{sp}\overline{|A|^2}, \tag{S5}$$

where Γ_{sp} is the relaxation rate of the space charge field and η_{sp} is the optical generation coefficient. Also, $\overline{|A|^2} = \frac{1}{t_R}\int_0^{t_R}|A|^2 d\tau$

is the round trip average power. Equation (S4) and (S5) form a complete set of equations describing Kerr comb generation under the influence of the photorefractive effect. We have neglected the thermo-optic effect since, as discussed in the main text, its effect is much smaller compared with the photorefractive effect. Numerically, Eq. (S4) is solved by the split-step Fourier method, where the time-dependent space-charge field is obtained from Eq. (S5) as

$$E_{sp}^{(m+1)} = (1 - \delta t \Gamma_{sp}) E_{sp}^{(m)} + \delta t \eta_{sp} \overline{|A|^2}, \tag{S6}$$

since the time step δt used for the split-step Fourier method is always much smaller than the photorefractive relaxation time $\frac{1}{\Gamma_{sp}}$.

In addition to the photorefractive effect described above, lithium niobate exhibits a pyroelectric effect [7]. Specifically, when an optical wave is launched into the resonator, photothermal heating (say, via material absorption) will increase the device temperature which in turn produces a material polarization and a space charge field that will blue shift the cavity resonance via the electro-optic effect. However, as the pyroelectricity-induced space charge field has a magnitude that is linearly proportional to the induced temperature increase, which in turn depends linearly on the optical power, Equation (S5) can still apply (although via an immediate temperature change). Therefore, while the time constants are slightly different, the photorefractive effect and the pyroelectric effect have a similar functional impact on the cavity resonance. For simplicity, we use Eq. (S5) to describe the overall effect, lumping them together as the "photorefractive effect".

C. Characterization of key parameters

Numeric modeling via Eqs. (S4) and (S6) requires detailed information about the device parameters. The linear properties, such as cavity Q, external coupling, and GVD, can be obtained from linear characterization of the device as described in the previous sections. The cavity length and the effective mode area are obtained from the finite element simulation of the device. The n_2 of lithium niobate was measured directly in our device via the threshold power of optical parametric oscillation, which is given by [1]:

$$P_{th} = \frac{\pi n \omega_0 A_{\text{eff}}}{4 \eta n_2} \frac{1}{D_1 Q^2}. \tag{S7}$$

The threshold power was determined by decreasing the on-chip pump power while scanning the wavelength quickly from blue to red until the onset of the parametric oscillation. The threshold power was thus measured to be 4.2 mW, and we determined the Kerr nonlinear coefficient to be $n_2 = 1.8 \times 10^{-19}$ m^2/W.

To determine the photorefractive response time constant, we employed a pump-probe approach [8, 9] where a sinusoidal modulation on a pump wave launched into a cavity mode modulates the refractive index which, in turn, is sensed by a weak probe wave launched into a separate cavity mode. The detailed experimental setup can be found in Ref. [9]. Figure S3 shows the recorded modulation response spectrum. The photorefractive effect exhibits a non-Lorentzian spectral response shape, indicating a potentially more complex (multi-time-constant) relaxation process, as is expected [6]. The modulation response exhibits a 3-dB bandwidth of about 20kHz, corresponding to a dominant relaxation time constant of $\sim$8 μs. For simplicity, we used this time response to describe the photorefractive dynamics as given in Eq. (S5).

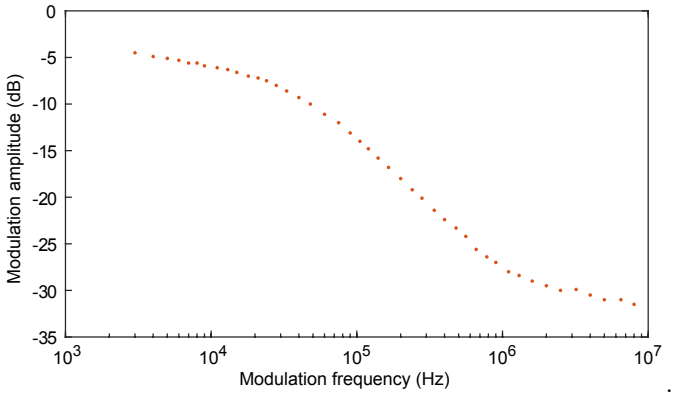

Fig. S3. The frequency response of the photorefractive effect.

Analysis of Eqs. (S4) and (S5) shows that the essential parameter governing the strength of photorefraction-induced cavity resonance tuning is $\rho_{pr} \equiv \frac{g_E \eta_{sp}}{\Gamma_{sp}}$. However, characterization of this parameter turns out to be quite complicated, since the field generation coefficient η_{sp} is power dependent [6]. This is particularly challenging during the Kerr comb generation since the intracavity field dynamics affect the overall intracavity energy (as shown in the next section). As such, we treat ρ_{pr} as a fitting parameter. Detailed modeling and analysis shows that a value of $\rho_{pr} = 8 \times 10^{-3}$ THz/W provides a reasonably good description of the system, and this value is used in the numerical modeling of comb generation.

D. Numerical modeling of soliton comb generation, power spikes and substructure

With the key parameters given above, it is possible to use Eqs. (S4) and (S6) to model the soliton comb generation via by the split-step Fourier method. A first example is meant to simulate the conditions in Fig. 3 of the main text wherein the pumping laser is tuned towards the cavity resonance from the red detuned side. This process was discussed in some detail in the main text and leads to power spikes followed by stable soliton generaion. Moreover, the power spikes consist of an unstable initiation followed potentially by a rapid cascade of higher to lower number soliton states. To simulate this process the pump power is set at 33 mW and the pump frequency is quickly tuned to a position that is one-half cavity-linewidth red detuned from the cold cavity resonance (Fig. S4(a)). Figure S4 shows the resulting simulated evolution of the comb generation process. When the pump frequency is tuned into the cavity resonance the intracavity optical energy initially grows (Fig. S4(d)) until the parametric oscillation threshold is attained. The oscillation quickly evolves into a broad spectral band via cascaded four-wave mixing (Fig. S4(b)), which creates a random waveform in the time domain (Fig. S4(f)). At the same time, the intracavity optical energy induces a photorefractive response that shifts the cavity resonance gradually towards the blue, leading to increased laser-cavity detuning ($|\Delta|$ increases) (Fig. S4(c)). Around a time of $t_1 = 1.2$ μs, the laser-cavity detuning has shifted to a value ($\Delta(t_1) \equiv \omega_p - \omega_0(t_1) = -3.6\ \Gamma_t$) that is large enough to allow the comb to transit into a breather soliton state (Fig. S4(b),(g)). This results in a rapid decrease of the intracavity energy (Fig. S4(d)). However, the photorefractive response is still strong enough to continuously blue shift the cavity resonance. The resulting gradual increase of cavity-laser

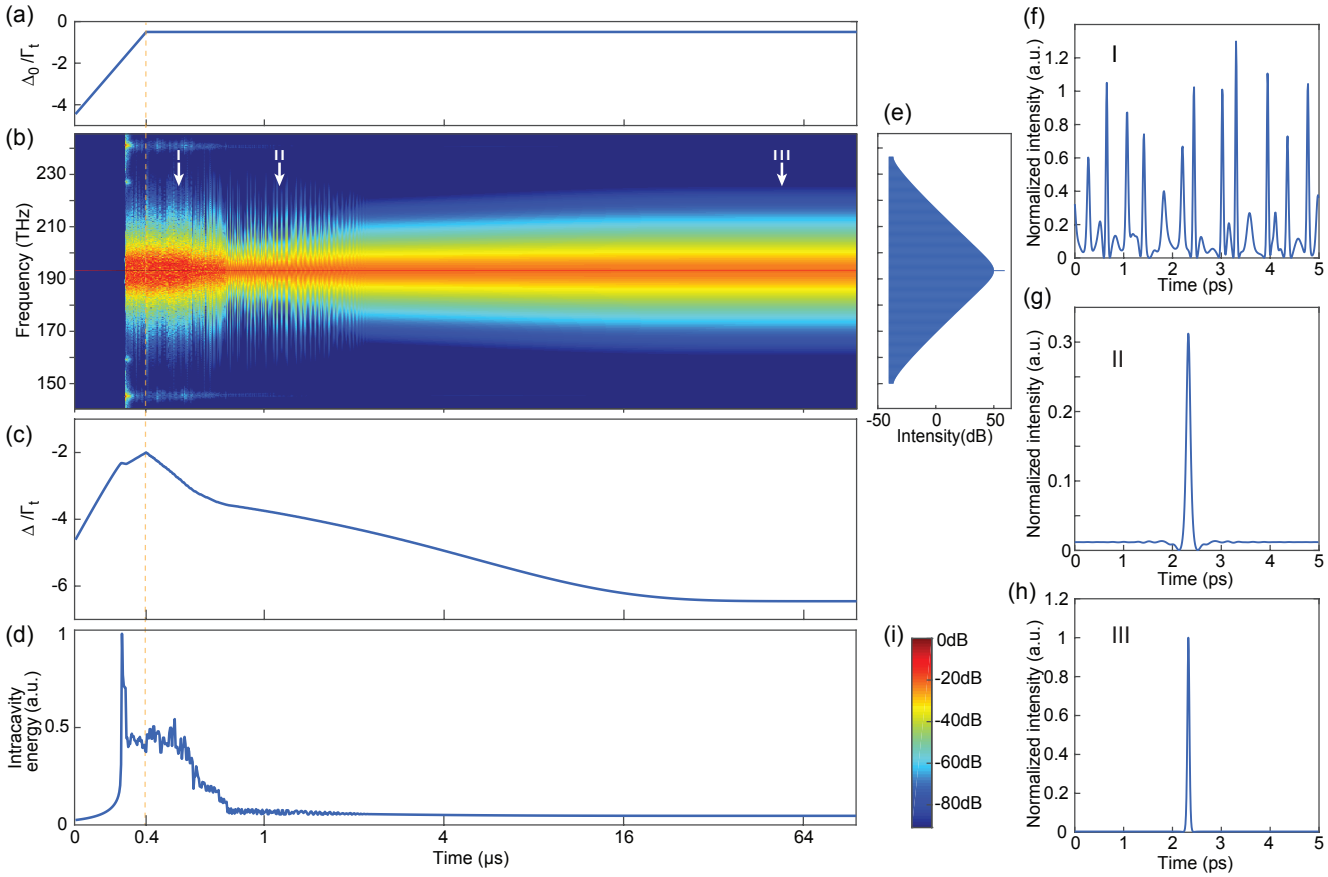

Fig. S4. Numerical modeling of the self-starting mode locking process. (a) Time dependence of the input pump frequency. The pump frequency is tuned linearly within 0.4 μs to a value of a value of $\omega_p - \omega_0(t_0) = -\frac{\Gamma_t}{2}$ ($t_0 = 0.4\ \mu s$) and remains constant afterwards, where Γ_t is the linewidth of the loaded cavity and $\omega_0(0)$ is the resonance frequency of the passive cavity in the absence of the input power. The pump power is fixed at 33 mW. **(b)** Simulated comb spectrum as a function of time within 100 μs. The corresponding color bar is shown in (**i**). **(c)** Laser-cavity detuning, $\Delta \equiv \omega_p - \omega_0(t)$ (normalized by Γ_t), as a function of time where $\omega_0(t)$ is the time-dependent cavity resonance under the photorefractive effect. **(d)** Intracavity energy as a function of time. Note that in (**a**)-(**d**) the horizontal time scale is set to be a linear scale within the initial 0-0.4 μs so as to show the detailed tuning of pump frequency and increase of intracavity energy, but to be a log scale within (0.4-100) μs to show the detailed evolution of the mode locking process. **(e)** Simulated spectrum of the mode-locked single soliton state at 100 μs showing a sech^2 spectral shape. **(f)-(h)** Temporal waveforms of the intracavity optical field at three different times indicated by the arrow I-III in (**b**). The intensities of three figures are all normalized to the peak intensity of the single soliton in (**h**). **(i)** Color bar for (**b**).

detuning causes the soliton spectrum to broaden by a certain extent. Eventually, around $t_2 = 41\ \mu s$, the cavity resonance settles to a stable value (Fig. S4(c)), resulting in a stable mode locked single-soliton state (Fig. S4(h)).

Figure S4 describes the condition in which a power spike (see main text discussion) evolves immediately into a single soliton state. However, as observed in Fig. 3 of the main text, there can also be meta-stable soliton states within the spikes. Importantly, these states are also observed in the numerical modeling. This is shown in the example of Fig. S5, where the photorefractive effect causes the Kerr comb to transit first into a three-soliton state that exists over a short time period of 1.6 μs before eventually transiting into a stable single soliton.

E. Discussion

The analysis in the previous sections reveals the underlying mechanism of the self-starting process of soliton mode locking in our device and the essential role played by the photorefractive effect. However, it should be noted that it is based upon a simplified single-relaxation model of the photorefractive effect (Eq. (S5)) with a constant field generation coefficient. As shown in Fig. S3, the frequency response of photorefraction is complicated with potential multi-time-scale responses [5]. Moreover, the field generation coefficient could be power dependent [6]. All these factors might impact the exact behavior of the self-starting soliton mode locking and requires further exploration in the future.

REFERENCES

1. X. Yi, Q.-F. Yang, K. Y. Yang, M.-G. Suh, K. Vahala, "Soliton frequency comb at microwave rates in a high-Q silica microresonator," Optica **2**, 1078 (2015).
2. L. A. Lugiato, R. Lefever, "Spatial dissipative structures in passive optical systems," Phys. Rev. Lett. **58**, 2209 (1987).
3. S. Coen, H. G. Randle, T. Sylvestre, M. Erkintalo, "Modeling of octave-spanning Kerr frequency combs using a

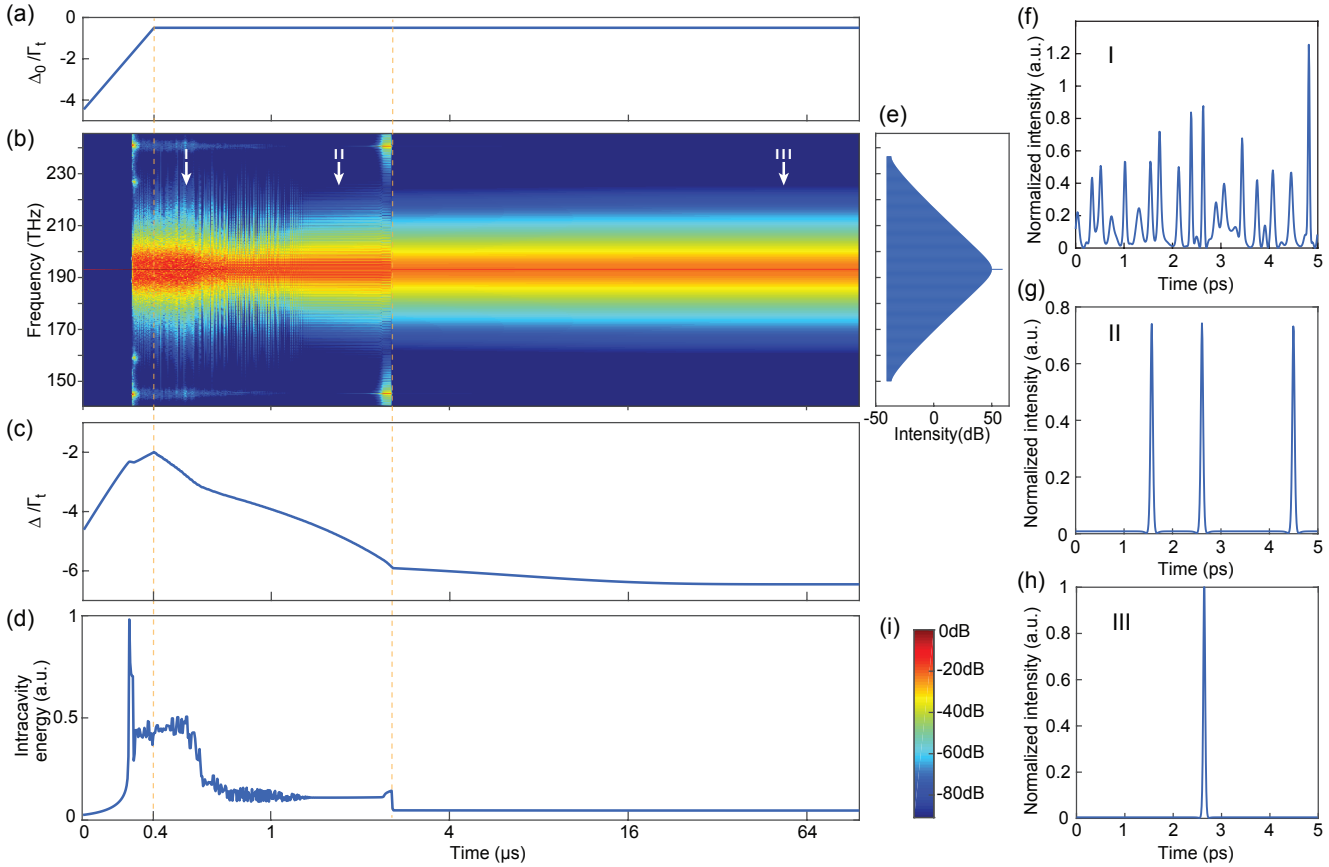

Fig. S5. Numerical modeling of the self-starting mode locking process. Same as Fig. S4 but showing an intermediate multi-soliton state.

generalized mean-field Lugiato-Lefever model," Opt. Lett. **38**, 37 (2013).

4. S. Coen, M. Erkintalo, "Universal scaling laws of Kerr frequency combs," Opt. Lett. **38**, 1790 (2013).
5. P. Günter, J.-P. Huignard, A. M. Glass, *Photorefractive materials and their applications*, vol. 1,2 (Springer, 1988).
6. X. Sun, H. Liang, R. Luo, W. C. Jiang, X.-C. Zhang, and Q. Lin, "Nonlinear optical oscillation dynamics in high-Q lithium niobate microresonators," Opt. Express **25**, 13504 (2017).
7. R. Weis, T. Gaylord, "Lithium niobate: Summary of physical properties and crystal structure," Appl. Phys. A **37**, 191 (1985).
8. H. Rokhsari, K. J. Vahala, "Observation of Kerr nonlinearity in microcavities at room temperature," Opt. Lett. **30**, 427 (2005).
9. X. Lu, J. Y. Lee, S. Rogers, Q. Lin, "Optical Kerr nonlinearity in a high-Q silicon carbide microresonator," Opt. Express **22**, 30826 (2014).
10. T. Herr, V. Brasch, J. D. Jost, C. Y. Wang, N. M. Kondratiev, M. L. Gorodetsky, and T. J. Kippenberg, "Temporal solitons in optical microresonators," Nat. Photon. **8**, 145 (2014).